Experiments in Fluids (2024) 65:187
https://doi.org/10.1007/s00348-024-03917-7

RESEARCH ARTICLE

Experimental investigation on boundary-layer streaks induced by grid-generated free-stream turbulence in a water channel

Tristan M. Römer[1] · Markus J. Kloker[1] · Ulrich Rist[1] · Christoph Wenzel[1]

Received: 18 July 2024 / Revised: 11 October 2024 / Accepted: 28 October 2024 / Published online: 3 December 2024

Abstract
In this study, the influence of various turbulence-grid configurations is analysed on both the induced free-stream turbulence (FST) and the resulting Klebanoff modes/streaks developing in a laminar flat-plate boundary layer downstream in a laminar water channel. All results are based on hot-film and particle image velocimetry measurements as well as visualizations. The grid design and installation has been done according to common grid installation recommendations to ensure homogeneous FST causing meandering Klebanoff modes inside the boundary layer. But it was found that (i) the Klebanoff modes do not meander for all grid configurations, (ii) not all configurations cause Klebanoff modes with the expected temporal and spatial behaviour, and (iii) for some configurations, the spanwise streak spacing is strictly locked to the grid spacing (mesh width). As these observations are unreported in the literature, this study is aimed at a thorough description of the influence of key grid parameters on the FST and the resulting streaks within the boundary layer. The investigation includes the grid parameters typically reported, such as the grid-bar diameters, the associated Reynolds numbers, or the streamwise placement of the grid, but now also the grid-orientation order (horizontal/vertical or vertical/horizontal order of grid bars of the dual-plane grid), the wall-normal position of the horizontal bars relative to the leading edge of the flat plate, and the existence of palpable imperfections in the manufactured grids. The Reynolds-number range covered lies well in the lower band of wind-tunnel experiments. Thus, this study suggests that the reliability and reproducibility of future experimental studies on FST would be greatly improved if they demonstrated homogeneity in the free-stream in both spanwise and wall-normal directions, documented the ongoing meandering and wavelengths of the generated Klebanoff modes and thus (implicitly) documented the spanwise independence of the results in the temporal mean. The latter is a prerequisite for the reliable investigation of FST/isolated-roughness interactions.

Graphical abstract

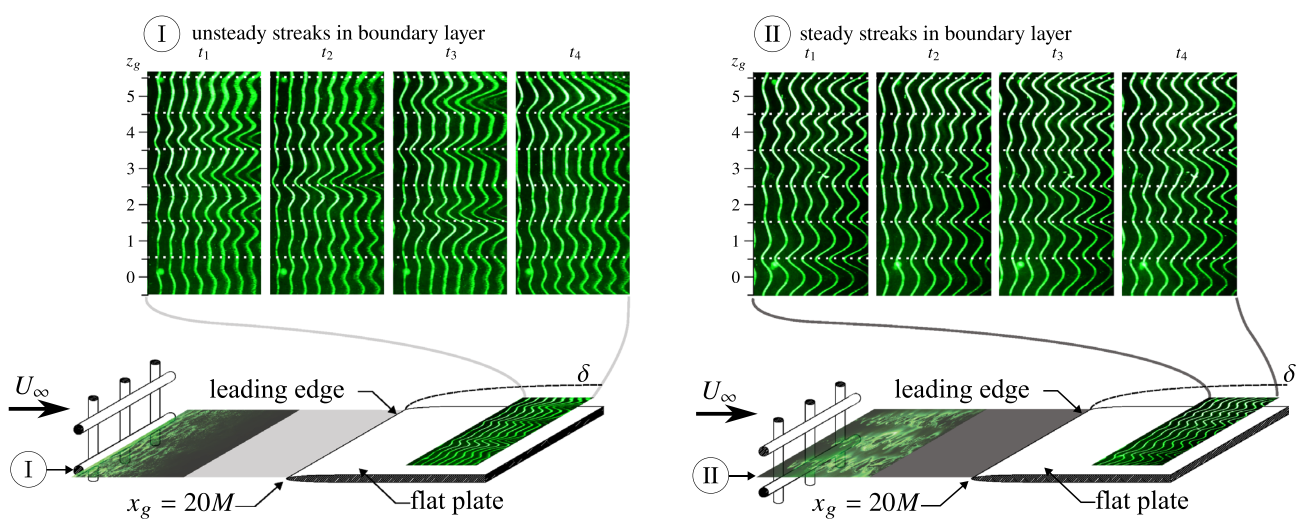

Extended author information available on the last page of the article

1 Introduction

It is known for many years that free-stream turbulence (FST) is one of the most dominant influencing factors for the laminar–turbulent transition process. For very small levels of FST, the laminar–turbulent transition of e.g. a flat-plate boundary layer (BL) is characterized by the exponential growth of initially small Tollmien–Schlichting (TS) waves, followed by a three-dimensional secondary instability that finally leads to laminar breakdown (Tollmien 1928; Schlichting 1933). For increased levels of FST, in contrast, the transition process can take different 'paths to turbulence', see Morkovin et al. (1994), partly hiding or replacing the classical TS-type transition. Essentially, algebraically growing streamwise velocity streaks are then generated in the boundary layer, often referred to as Klebanoff modes (Ellingsen and Palm 1975; Kendall 1985; Gustavsson 1991), which meander in the spanwise direction and can undergo a secondary instability of the sinuous or varicose type (Andersson et al. 2001), see Sect. 2.1 for a more detailed introduction.

Due to its high relevance for practical applications, FST has been investigated widely (see Sect. 2), and our understanding is fairly advanced nowadays. The turbulence level *Tu* alone is known to be not satisfactorily characteristic, but also the frequency content and the integral length scale play a role.

In many experimental studies, FST is generated by a rectangular grid upstream of the leading edge (LE) of the plate or body, where the grid spacing, the grid bar diameter and distance: grid-LE should follow well-proven value ranges gained by numerous studies, see Sect. 2 for more details.

1.1 Motivation

It is an essential characteristic of Klebanoff modes to meander, and their spatial appearance is random. In the temporal mean, the meandering appearance cancels out and makes the timewise mean flow independent of the spanwise location. Naturally, turbulence grids with their cohering vertical and horizontal grid bars are fixed in their spatial position, so the spatial flow perturbation has a timewise constant part, at least in the near wake. The situation is similar to what Klebanoff did by putting spanwise-periodic spacers on the plate to fix the spanwise meandering motion he observed in his transition studies on what is today known as K-breakdown. At some distance downstream, in the turbulent boundary layer, the effect of the spacers (and the longitudinal vortex modes) vanishes, and the turbulence is homogeneous in the spanwise direction. With FST grids, the free-stream has such a steady three-dimensional (3D) structure initially and it is not clear a priori whether this structure dies out quickly enough in any case not to play a leading role in the transition process. However, most experimental studies neither discuss the actual meandering of the streaks nor ensure the spanwise independence of the measurement results. While this may not necessarily cause problems for the FST generated transition, statistically balanced meandering is elementary for reliable investigations of roughness-element-induced transition with FST. With a roughness element, it makes a significant difference whether the roughness element is permanently located in a high- (or low-) speed streak, or stochastically hit by meandering high- and low-speed streaks. Consequently, it must be ensured that the elements are equally affected by both high- and low-speed streaks, or otherwise the results depend on the spanwise position of the elements with respect to the used turbulence grid.

1.2 Objectives of the study

In preparation for FST-related studies in the open-surface laminar water channel (LWC) at Institute of Aerodynamics and Gas Dynamics (IAG), FST-grids were constructed and installed based on common criteria (see Sect. 2.3). To clearly characterize the resulting flow field, a measurement campaign has been carried out in which both the turbulent free-stream and the resulting Klebanoff modes (BL-streaks) were measured and visualized. Hereby, the following observations have been made:

1. The Klebanoff modes did not meander for all grids/grid setups.
2. For some grids, the Klebanoff mode's spanwise wavelength appeared to be both spatially and temporally locked to the grid spacing *M*.
3. For some grids, the Klebanoff mode's spanwise wavelength appeared locked to twice the grid spacing (2*M*).
4. In general, the Klebanoff modes were found to be extremely sensitive to numerous, sometimes minimal, differences between different turbulence grids.

For visualization, the graphical abstract gives a time series of snapshots of hydrogen-bubble visualizations from the BL in top view for the same FST grid but placed at two different wall-normal positions. While transient, meandering streaks develop for the grid mounting position I (left figure), stationary streaks develop when the grid is shifted upwards by half the grid spacing, mounting position II (right figure). The timelines indicate the positions of the low- and high-speed streaks.

It is the main goal of this study to investigate the influence of the vertical positioning of the turbulence grid in relation to the LE of the plate, the Reynolds number, the bar diameter, the grid-orientation order, as well as the existence of small imperfections like tiny welding points that connect the horizontal and vertical grid bars. By doing so, a general understanding can be established about aspects that need to be considered in both the design and the installation of FST-grids, and to raise awareness of the high sensitivity the FST can have to the setup used at extreme cases. It can be seen as a particular advantage of the water channel used that the meandering motion of the Klebanoff modes is easier to visualize compared to wind tunnels, where the methods for properly detecting the meandering motion (e.g. Schlieren visualization) are very demanding, a situation that is further enhanced by the larger time and length scales present in the water channel.

The paper is structured as follows First, the background from the literature is summarized in Sect. 2, before the experimental setup/method is introduced in Sect. 3. Subsequently, the influences of the grid on the free-stream conditions are discussed in Sect. 4, before the resulting characteristics of the Klebanoff modes are discussed in Sect. 5. Finally, a summary is given in Sect. 6.

2 Background

2.1 Influence of FST on the transition process

According to the *roadmap to turbulence* by Morkovin et al. (1994), different linear and (weakly) nonlinear stages in the boundary layer are passed or bypassed, depending on the power of the internal or external disturbances (Saric et al. 2002). External disturbances, such as FST, interact with the boundary layer through a receptivity process, as shown experimentally by e.g. Westin et al. (1994) and numerically by Jacobs and Durbin (2001) or Brandt et al. (2004). This process can be described as a filtering process, usually referred to as *shear-sheltering* (Hunt and Durbin 1999), which only allows low-frequency disturbances to penetrate into the boundary layer, see e.g. Zaki (2013). Inside the boundary layer, the low-frequency distortions push high-momentum fluid from the upper part of the boundary layer towards the wall, which vice versa causes a lifting of low-momentum fluid from the wall due to continuity, similar to what counter-rotating steady longitudinal vortex pairs do. Usually, this mechanism is known as the *lift-up effect* (Landahl 1980) and causes a cross-sectional fluid motion subsequently resulting in boundary-layer streaks. These streamwise velocity streaks grow algebraically and transiently in their streamwise evolution, and are often referred to as Klebanoff modes (Ellingsen and Palm 1975; Kendall 1985; Gustavsson 1991). An algebraic growth of a disturbance is described by non-modal theory, thus making the Klebanoff mode not to be a(n exponentially growing eigen-) mode in a strict sense. Due to the random behaviour of the FST, the Klebanoff modes are unsteady and meander randomly in the spanwise direction. In principle, however, streaks can also be steady (Mandal et al. 2010), for example, when streaks are triggered by a roughness element. The Klebanoff modes can undergo a secondary instability of the sinuous or varicose type (Andersson et al. 2001), depending on their amplitude, as exemplarily demonstrated in the LWC by dye-tracing visualization in Fig. 1; eventually turbulent spots result randomly leading to a turbulent BL downstream. More details on the breakdown process can be found in the numerical studies by e.g. Jacobs and Durbin (2001), Brandt et al. (2004), Ovchinnikov et al. (2008) and Ohno et al. (2023), the experimental studies by Westin et al. (1994) and Matsubara and Alfredsson (2001), the combined numerical and experimental study by Schlatter et al. (2008) and the review by Saric et al. (2002).

2.2 Empirical estimations

In the prediction of the FST-induced transition location, it is a main difficulty that not only the turbulence intensity

$$Tu = \frac{u'_{\mathrm{rms}}}{\bar{u}}, \tag{1}$$

with u'_{rms} the root-mean-square (RMS) of the velocity fluctuation u' and $\bar{u}$ the mean velocity (e.g. Hislop (1940); Blair and Werle (1980); Matsubara and Alfredsson (2001)), but also the integral length scale Λ_x strongly affect the actual transition location (Fransson et al. 2005; Fransson and Shahinfar 2020). Assuming Taylor's hypothesis of *frozen* turbulence, the streamwise integral length scale

$$\Lambda_x = \bar{u} \int_0^\infty f(\tau) d\tau \tag{2}$$

is defined by the auto-correlation function $f(\tau)$ with respect to the time lag τ, see also Fuchs et al. (2022) for further discussion. In an effort to derive a comprehensive transition prediction which both takes Tu and Λ_x at the LE into account, Fransson and Shahinfar (2020) recently proposed a semi-empirical transition model based on

$$Re_{\mathrm{FST}} = \frac{u'_{\mathrm{rms}} \Lambda_x}{\nu}, \tag{3}$$

with ν the kinematic viscosity. Besides the transition location, the averaged streak spacing λ_z can be estimated to be

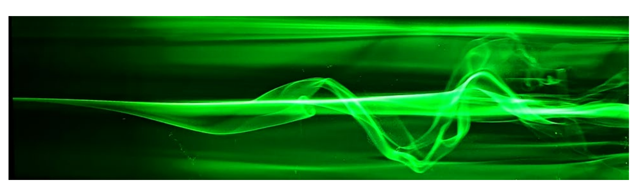

Fig. 1 Top view (flow from left to right) of a visualization with fluorescent dye (uranine) in the boundary layer subjected to FST, showing a secondary instability

around $\lambda_z = 6\delta_1$ (δ_1 is the displacement thickness), Matsubara and Alfredsson (2001), which coincides about with the spacing of the strongest transiently growing steady streaks found in theoretical studies without FST. On the other hand,

$$\lambda_z = \Lambda_x Tu\left(c_1 Re_{\mathrm{FST}}^{-1/\sqrt{2}} + c_2\right)^2 \tag{4}$$

has been proposed by Fransson and Shahinfar (2020); the constants $c_1 = 186$ and $c_2 = 0.8$ are calibrated (for air). Note that prediction (4) does not contain any boundary-layer scale and may apply in cases where no direct relevant boundary-layer reaction, by transient growth for example, occurs.

2.3 Grid-generated FST

In FST experiments, it is a common procedure to increase the level of FST by installing grids well ahead of the measuring section, which are mostly passive with bars. For the basic square grids with round bars, the resulting FST conditions are usually determined by the three geometrical parameters (Kurian and Fransson 2009): (i) the grid spacing (mesh width) M, (ii) the bars' diameter d, and (iii) the grid's porosity β (Roach 1987), which is the ratio between the open and the total area of the grid

$$\beta = (1 - d/M)^2. \tag{5}$$

On the one hand, to avoid large-scale mean velocity variations which can remain far downstream of the grid (Kurian and Fransson 2009), the porosity β is usually recommended to be larger than 0.55. On the other hand, too high values can increase the downstream distance of inhomogeneity (Mohamed and Larue 1990). In short, the influence of the turbulence grids on the resulting FST can be summarized as follows: (i) The lower the porosity, the higher Tu (Fransson and Shahinfar 2020). (ii) The integral length scale (Λ_x) scales with M, as shown by e.g. Kurian and Fransson (2009). (iii) Thicker bars lead to higher FST at the LE at a given streamwise grid position (Batchelor and Townsend 1948). (iv) Furthermore, a grid is characterized by the Reynolds numbers

$$Re_d = \frac{ud}{\nu}, \tag{6a}$$

$$Re_M = \frac{uM}{\nu}. \tag{6b}$$

Re_d must be larger than 80 to increase the natural FST (Mehta 1985), lower values have the effect of a quietening, Tu reducing screen. In general, a lower Reynolds number leads to an earlier homogeneous turbulence behind a particular grid (Kurian and Fransson 2009).

The distance between the grid and the plate's LE plays a decisive role in the felt turbulence: (i) First, the FST level decreases with increasing distance from the grid due to dissipation. The decay of grid-generated FST can be expressed by:

$$Tu = \sqrt{A\left(\frac{x_g - x_{g,0}}{M}\right)^b} \tag{7}$$

from thereon, see Batchelor and Townsend (1948). Here, $x_{g,0}$ denotes a virtual origin of the grid, b the decay rate and A an individual constant for a particular grid and Re. (ii) Second, the (streamwise) integral length scale increases with increasing distance from the grid due to the different fade-out of larger and smaller wavenumbers $\alpha = 2\pi/\lambda_l$, where λ_l is the wavelength. This behaviour of 'dying' turbulence with absent turbulence production can be illustrated most tangibly by considering a wave-like disturbance

$$u_e(x) \propto e^{i\alpha x}, \tag{8}$$

where i is the imaginary unit. The second derivative of Eq. (8) is

$$u_e(x)'' \propto -\alpha^2 e^{i\alpha x}, \tag{9}$$

which provides the viscous damping of the wave, implying that high values of α (low values of λ_l) are disproportionately damped compared to low values of α (high values of λ_l) for dying turbulence outside a shear layer. Thus, smaller vortices decay faster than larger ones, and since the integral length scale can be interpreted as the averaged eddy size of the turbulence (Camp and Shin 1995), the relative length scale in streamwise direction increases.

2.4 Homogeneous FST

Only if the generated wakes behind every respective neighbouring bar of the grid sufficiently interact with each other, homogeneous (and isotropic) FST can be achieved. We define the FST at a certain streamwise position x_1 downstream of a grid as homogeneous, if:

$$\left.\frac{\bar{\boldsymbol{u}} - U_\infty}{U_\infty}\right|_{x_1,y_1,z_1} = \left.\frac{\bar{\boldsymbol{u}} - U_\infty}{U_\infty}\right|_{x_1,y_2,z_2}, \tag{10a}$$

$$\Lambda_x(x_1, y_1, z_1) = \Lambda_x(x_1, y_2, z_2), \tag{10b}$$

$$\left.\frac{\boldsymbol{u}'_{\mathrm{rms}}}{U_\infty}\right|_{x_1,y_1,z_1} = \left.\frac{\boldsymbol{u}'_{\mathrm{rms}}}{U_\infty}\right|_{x_1,y_2,z_2}, \tag{10c}$$

where U_∞ is the free-stream velocity.

As a rule of thumb, homogeneity is often found to occur for distances larger than $20M$ downstream of a grid (see e.g. Alfredsson and Matsubara (2000); Mandal et al. (2010), concluded by Groth and Johansson (1988)). In fact the minimum distance depends on M, d, Re_M and other parameters, as mentioned in Roach (1987); Lavoie et al. (2007); Kurian and Fransson (2009) and shown in the following.

3 Experimental methods

3.1 Experimental facility and measurement equipment

All the following experiments were conducted in the closed-loop LWC at IAG at the University of Stuttgart, $Tu = 0.05\,\%$ between 0.1 and 10 Hz at velocity $U_\infty = 0.1\,\mathrm{m\,s^{-1}}$, see Wiegand (1996); Puckert et al. (2017). It has a test section of $10 \times 1.2 \times 0.2\,\mathrm{m}^3$. An 8 m long flat plate with an elliptical nose is permanently installed at a height of 0.05 m above the bottom of the test section, whereby the pressure gradient can be adjusted to zero by a mesh at the end of the test section. The measurements were taken using a Dantec 55R15 single and a 55R61 X hot-film probe with a 3D traverse system. The Dantec‚ Streamline‘ bridge is connected to the hot-film probes, which operates based on the constant-temperature-anemometry principle. The output voltage is recorded using a 16-bit National Instruments USB-6216 A/D converter, and converted to velocity u using King's law. To determine the King's law constants, the hot-film probes are calibrated by traversing through resting water at various speeds. The calibrated velocity and the one obtained by hydrogen-bubble time-lines (more details see below) are in good agreement and presented for example by Puckert et al. (2020). Both probes are operated with a sampling rate of $f = 100\,\mathrm{Hz}$ without filtering to capture high-frequency disturbances correctly. A discussion about the validity of this sampling rate can be found in e.g. Shin et al. (2015). The single hot-film probe is used for measurements in the boundary layer and above, the X-probe for measurements behind the grids. For the latter, the absolute velocity is $\boldsymbol{u} = \sqrt{u^2 + w^2}$, printed in bold. For the X-Probe decomposition into the velocity components, an individual yaw coefficient is used, which results in a maximum deviation of the captured and measured velocity angle of 1.7° within ±30° of the real velocity angle. The measurement uncertainties using the hot-film anemometry in the LWC are addressed by Puckert et al. (2020) and have been updated by Römer et al. (2023). Hydrogen-bubbles shed from a DC pulsed wire are visualized behind the grids and in the boundary layer with a laser light sheet. The wire has a diameter of 0.25 mm and a length of 200 mm and is operated at 400 Volt and 2.2 Ampere. Dye-tracing visualizations are performed with the fluorescein uranine and ultraviolet lamps at the sidewalls of the LWC. To identify the wavelengths of the boundary-layer streaks, particle image velocimetry (PIV) measurements are taken in wall-parallel planes within the boundary layer. A Q-switched dual-pulse Nd:YAG laser (Quantel Brilliant Twin W) with a wavelength of 532 nm and pulse rate of 2Hz is connected to a light-guiding arm and illuminates polyamide tracer particles of 4.2 µm diameter in a less than 1 mm thick wall-normal laser sheet. To capture the slow meandering of the streaks adequately, the relatively low pulse rate is chosen in order to optimally use the maximum camera (12-bit PCO SensiCam) memory of 180 double images at a resolution of 1280×1024 pixels. The camera is mounted perpendicular to the illuminated laser sheet at a distance of 0.6 m and is connected to the DLR (V3.2) sequencer together with the laser. Fresh water for the LWC is first decalcified by an iron exchanger to prevent deposits in the LWC and on the hot-film probes. In addition, the water is stored in a tank system for several days prior to being filled into the LWC, to obtain room temperature and degassing. This process avoids temperature Schlieren and prevents the adhesion of bubbles to the hot-film probes. More details on the LWC, hot-film anemometry and PIV can be found in Puckert (2019).

3.2 Grid properties

The grids used consist of round rods arranged in a square pattern, with the horizontal bars and the vertical bars being aligned in different planes ('dual-plane grid'), corresponding to the layout of the grids G1-G6 by Fransson and Shahinfar (2020)), for example. Three grid diameters were investigated ($d = 2$, 3 and 4 mm), with identical grid spacing ($M = 25$ mm); fulfilling the criteria introduced in Sect. 2.3 for the set free-stream velocities in the LWC, see Table 1. As it turned out, the particular way in which the joints between the horizontal and vertical bars are manufactured can greatly influence the resulting FST properties. Mainly due to the limited availability of prefabricated grids, these connections differ for each grid: (i) grid A ($d = 2$ mm) is a conventionally fabricated grid made of stainless steel, spot-welded by a machine, see Fig. 2a; (ii) grid B ($d = 3$ mm) is a custom-made grid made from stainless-steel bars that are welded by hand at every second crossing point, see Fig. 2b; (iii) for grid C ($d = 4$ mm), the horizontal and vertical grid bars are not connected to each other, though still touching each other, see Fig. 2c. To prevent the bars from bending, this grid is made of polished carbon-fibre bars that are rigidly clamped in an outer frame; for all experiments described below, it was ensured that the bars do not vibrate.

Table 1 Overview of the geometrical data and free-stream conditions for $\nu = 10^{-6}\,\mathrm{m^2s^{-1}}$, where the index 1 and 2 stands for the setup with free-stream velocity $U_{\infty,1} = 0.058\,\mathrm{m/s}$ and $U_{\infty,2} = 0.11\,\mathrm{m/s}$, respectively

Grid	Cross-intersection	d [mm]	M [mm]	β	$Re_{d,1}$	$Re_{d,2}$	$Re_{M,1}$	$Re_{M,2}$
A	Spot welded	2	25	0.846	116	220	1450	2750
B	Welded seam at every second intersection	3	25	0.774	174	330	1450	2750
C	Only touching	4	25	0.706	232	440	1450	2750

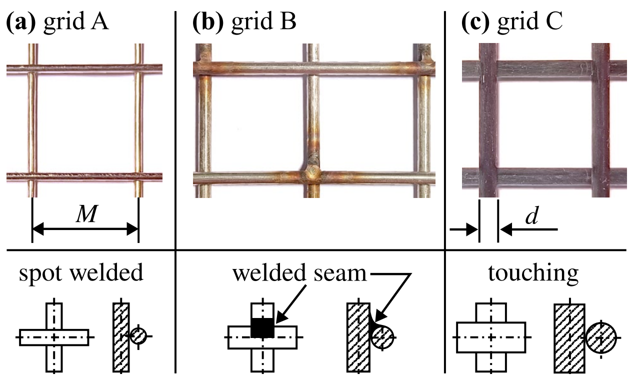

Fig. 2 Images of the grid structures (top) and detailed schematics of the grid intersection points (bottom)

The grid parameters Re_d, Re_M, β in Table 1 compare as follows to those in the literature, for example Tan-Atichat et al. (1982); Mehta (1985); Groth and Johansson (1988); Fransson et al. (2005); Mandal et al. (2010); Fransson and Shahinfar (2020); Mamidala et al. (2022). The lowest porosity $\beta = 0.706$ (grid C) is used rather frequently, e.g. grid G5 from Fransson and Shahinfar (2020) or grid C5 from Mamidala et al. (2022). Its parameter combinations are comparable to Fransson et al. (2005) ($\beta = 0.72$, $Re_d = 470$, $Re_M = 3087$ for $U_\infty = 2\,\mathrm{m/s}$ and $\nu_{\mathrm{air}} = 14.9 \cdot 10^{-6}\,\mathrm{m^2s^{-1}}$). The highest porosity (grid A, $\beta = 0.846$) is relatively high compared to the literature, but still cannot be considered exotic: Mandal et al. (2010) (grid 2) used a relatively similar grid with $\beta = 0.81$ or Mamidala et al. (2022) (grid C8) wit $\beta = 0.893$. Its parameter combinations can be found in e.g. Tan-Atichat et al. (1982); Mandal et al. (2010); Groth and Johansson (1988).

Grid C might be denoted as a more common choice with regard to the literature compared to grid A (in air). To be able to compare experiments in water and air, Re_d of the bars and Re_x of the measurement position on the plate should about coincide; that has been secured. Even though it turned out that the FST behaviour discussed below does not always coincide with the aforementioned experiments, the wall-normal grid position relative to the flat plate or different pressure-gradient conditions play a non-negligible role.

3.3 Experimental setup

The grid-related coordinate system (x_g, y_g, z_g), see Fig. 3, originates in the grid cell centre; $y_g = 0$ corresponds to the position between two horizontal bars, $y_g = 0.5M$ behind a horizontal bar. Similar holds for the spanwise position, see Table 2. The second coordinate system (x, y, z) originates

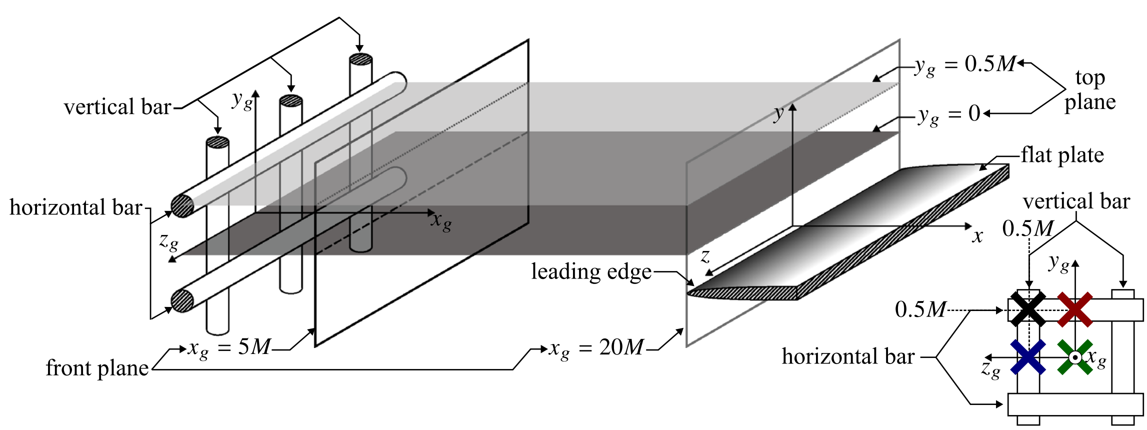

Fig. 3 Experimental setup in the LWC

Table 2 Measurement positions relative to the grid cell

	(y_g, z_g)	
×	(0,0)	Centre of a grid cell
×	(0.5, 0)	Behind a horizontal bar and between two vertical bars
×	(0, 0.5)	Behind a vertical bar and between two horizontal bars
×	(0.5, 0.5)	Cross section of a vertical and horizontal bar

at the LE of the flat plate. For all subsequent investigations, two wall-normal grid positions relative to the flat plate are investigated: (i) The LE is located behind a horizontal bar, and (ii) it is located between two horizontal bars.

The grids A and C have been installed in two succession orders (vertical–horizontal or horizontal–vertical in streamwise direction) and at the two vertical positions $y_g = 0$ or $y_g = 0.5M$, resulting in nine grid configurations, see Table 3; grid B has been applied just in one setting. Since all of these nine setups were applied at the two free-stream velocities given in Table 1 ($U_{\infty,1} = 0.058\,\mathrm{m/s}$ and $U_{\infty,2} = 0.11\,\mathrm{m/s}$ with $U_{\infty,2} \approx 2U_{\infty,1}$) to evaluate the effect of the Reynolds numbers Re_d and Re_M, a total of 18 setups are discussed in the following.

4 Results in the free-stream

4.1 Visualizations of the grid's near wake

To get a first impression of the flow field behind the turbulence grids, Fig. 4 summarizes hydrogen-bubble visualizations behind grids A and C for $0 \leq x_g \leq 5M$. For both grids A and C, both a vertical–horizontal grid order and a horizontal–vertical grid order are visualized, with the wire being either placed between two horizontal bars (left column, index I) or at the height of a horizontal bar (right column, index II). For all visualizations, $U_{\infty,2}$ has been set.

4.1.1 Influence of the grid diameter and wall-normal grid position relative to the flat plate

Only setups A-VH and C-VH are considered first.

For setup A-VH|0, Fig. 4a$_\mathrm{I}$ clearly shows typical structures of a Kármán vortex street behind the vertical bars, as expected for $Re_{d,2} = 220 > 40$ (Lienhard 1966). Although this principally also applies to setup C-VH|0 (Fig. 4c$_\mathrm{I}$), the vortices in the near wake of the vertical bars are more reminiscent of a Kelvin-Helmholtz instability caused by two separate shear layers for $x_g < 1M$ before they seemingly mutate into a Kármán vortex street further downstream. If the interaction of the wakes of neighbouring vertical grid bars is compared, an already good mixing appears for grid C at $x_g = 5M$, while the wakes of grid A have almost not mixed at all at $x_g = 5M$. If the flow field behind the horizontal bars is compared, setups A-VH|0.5 and C-VH|0.5, both are much more mixed, whereby the top view of setup A-VH|0.5 simply represents a bar-parallel slice through the rather two-dimensional vortices induced by the cylinder, see Williamson (1996).

Consequently, the visualizations from Fig. 4 suggest that a significantly earlier spanwise homogenization of the grid's wake can be expected in planes behind horizontal bars rather than between two horizontal bars, which does not necessarily have to be completely balanced for every grid diameter d at a streamwise position of $x_g = 20M$. Accordingly, it seems possible that for unfavourably selected grid configurations, the wall-normal mounting position of the grid with respect to the plate's LE indeed can have a noteworthy influence on the resulting Klebanoff modes that will emerge on the flat plate later on. (Note that δ/d scales with $\sqrt{Re_x/Re_d}$.) Obviously, this is more likely for thinner grid bars compared to thicker bars, where the mixing of the wakes is stronger.

Table 3 Overview of the setups

Grid	Setup def. 1	Orientation	Setup def. 2	FS: measurement height BL: height of LE
A	A-VH	Vertical–horizontal	A-VH|0	Between two horizontal bars
			A-VH|0.5	Behind horizontal bar
	A-HV	Horizontal–vertical	A-HV|0	Between two horizontal bar
			A-HV|0.5	Behind horizontal bar
B	B-VH	Vertical–horizontal	B-VH|0	Between two horizontal bars
C	C-VH	Vertical–horizontal	C-VH|0	Between two horizontal bars
			C-VH|0.5	Behind horizontal bar
	C-HV	Horizontal–vertical	C-HV|0	Between two horizontal bars
			C-HV|0.5	Behind horizontal bar

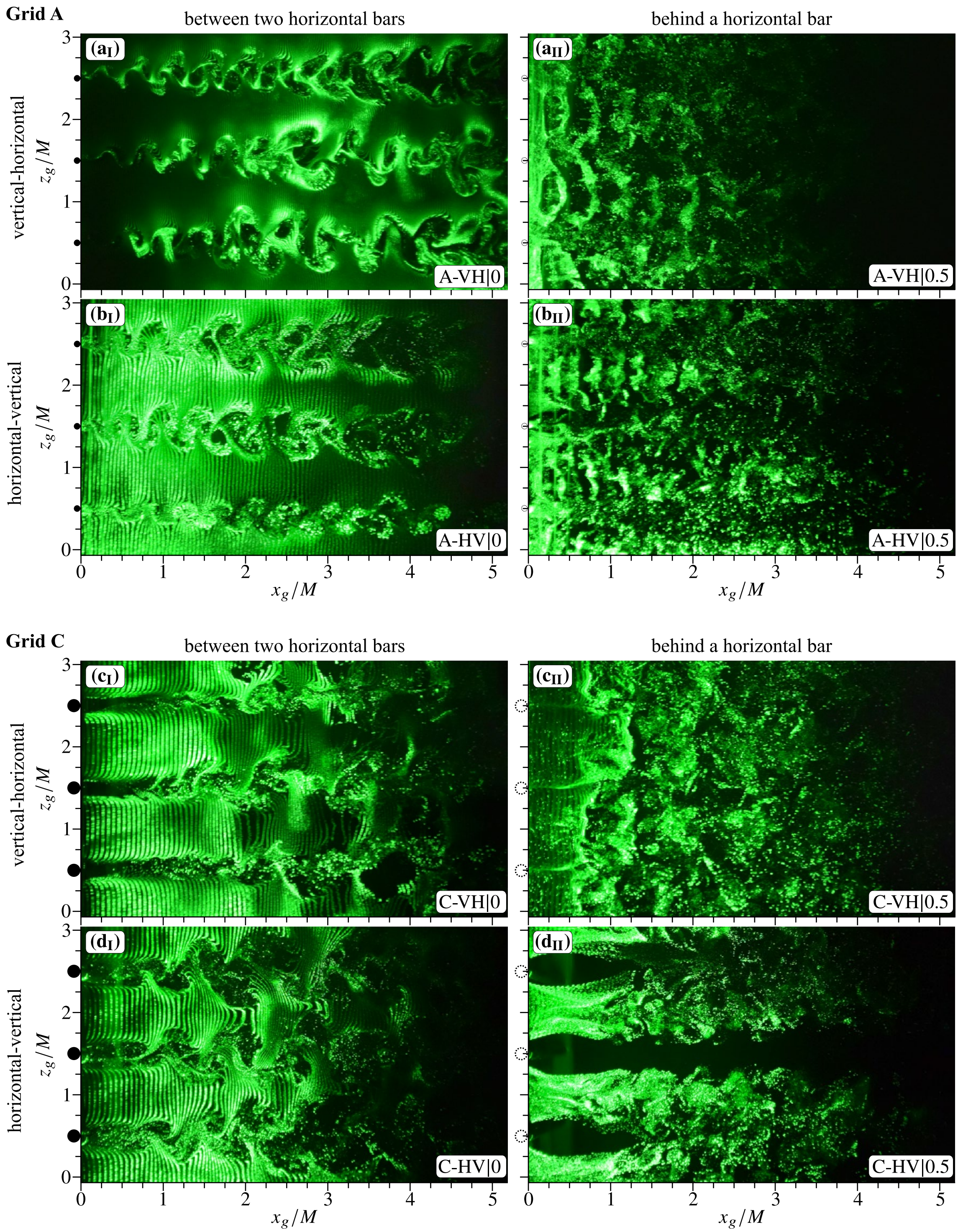

Fig. 4 Hydrogen-bubble visualization behind grid A (top four figures) and grid C (bottom four figures) in the view from above. Each row is either visualized in the vertical–horizontal or horizontal–vertical order. The left columns and the right columns show the flow field between two horizontal bars ($y_g = 0$) and behind a horizontal bar ($y_g = 0.5M$), respectively. The black dots on the z_g axis indicate the size and positions ($z_g = \{0.5, 1.5, 2.5\}M$) of the vertical bars

4.1.2 Influence of the grid-orientation order

The influence of the bar-order can be seen by comparing the pictures in the first column in Fig. 4 for grids A and C. Setups A-VH|0 and A-HV|0 do not show significant differences; the same applies setups C-VH|0 and C-HV|0. If the results behind the horizontal bars are compared, right column, grid C shows however clearly pronounced recirculation regions behind the horizontal bars, with a spanwise extension of almost $0.5M$. As expected, the spanwise extension of these recirculation regions strongly decreases for smaller grid diameters and are only barely visible for grid A, setups A-VH|0.5 and A-HV|0.5.

Hence, the visualizations from Fig. 4 suggest that the grid diameter, the wall-normal grid position relative to the flat plate as well as the grid-orientation order might play a non-negligible role on the FST conditions at the beginning of the flat plate, $x_g = 20M$.

4.2 Measurements of the FST characteristics

X-probe measurements for $0 \le x_g \le 20M$ have been taken to assess the homogeneity of the FST at the LE of the flat plate. In accordance with the previous chapter, only grids A and C are discussed in the following, which have minimum and maximum grid diameters, respectively. All plot setups will be introduced in Sect. 4.2.1 first.

4.2.1 Introduction of Figs. 5 and 6

In the same representation for all later-discussed grid setups, the results of the X-probe measurements are depicted in Fig. 5 according to the measurement setup in Fig. 3. Here, the two respective contour plots on the left side (index I and index IV) in Fig. 5 show the mean flow velocity according to Eq. (10a) in top view (x_g/z_g-plane), whereby the upper plot (index I) represents the flow field at a height between two horizontal bars ($y_g = 0$), while the lower plot (index IV) represents it at a height of a horizontal bar ($y_g = 0.5M$). To further illustrate the flow field perpendicular to the flow direction, two planes in front view (y_g/z_g-plane) are depicted in the middle row of Fig. 5, a first one evaluated at $x_g = 5M$ (index II) and a second one at $x_g = 20M$ (index V). Note that different contour levels were selected for the region between $0 < x_g/M \le 6$ and $6 < x_g/M \le 20$ to visually emphasize effects more strongly which otherwise would be hidden due to the strong variation of the velocity fields in the streamwise direction. To additionally enable a quantitative evaluation of the spanwise variation of the flow fields, the two respective right-hand plots in Fig. 5 (index III and VI) present the velocity profile in the spanwise direction for each grid setup at $y_g = 0$ and height of $y_g = 0.5M$. While the blue lines are evaluated at $x_g = 5M$, the red lines are evaluated at $x_g = 20M$. To enable statistical statements about the development of the FST properties in the streamwise direction, Fig. 6 depicts both the development of the mean velocity in the left panels (index I) and the fluctuation amplitude in the right panels (index II). Instead of the local mean velocity $\bar{\boldsymbol{u}}$ usually used in the literature to calculate Tu (see Eq. (1)), U_∞ is used here, as this provides a better comparison between the setups. Qualitatively, there are no differences in the results based on the definition. Due to the strong randomness of the generated FST in the near wake ($x_g < 10M$), the mean velocity values given in Figs. 5 and 6 exhibit quantitatively slight discrepancies relative to each other, especially at the sensitive position behind the intersection of a vertical and horizontal bar (✕ in Fig. 3).

4.2.2 FST characterization behind grid A-VH

The visualization in Fig. 4 showed clearly pronounced Kármán vortex streets at the height between two horizontal grid bars (A-VH|0), which only intermingled slowly with each other in their streamwise evolution. As can be seen from Fig. 5$\mathrm{a_I}$, these vortex streets cause clearly recognizable low-speed and high-speed jets in the mean-flow field, which are still clearly visible at $x_g = 20M$. Although the measuring plane at the height of a horizontal bar (A-VH|0.5) in 5$\mathrm{a_{IV}}$ shows a much more uniform velocity field that is slightly slower with respect to the incoming velocity $U_{\infty,2}$, a distinct grid structure is also recognizable here. Remarkably, these inhomogeneities lead to an almost perfect rectangular distribution of the mean velocity in the planes perpendicular to the flow direction in Fig. 5$\mathrm{a_{II}}$, which strictly correlate with the grid cell geometry. Even if this pattern weakens considerably in the streamwise direction (see Fig. 5$\mathrm{a_{III}}$, $\mathrm{a_V}$, $\mathrm{a_{VI}}$), a variation of the mean-velocity distribution of around ±2% is still present at $x_g = 20M$ between two vertical bars. It is interesting to see from Fig. 6$\mathrm{a_I}$ that the main cause of this inhomogeneity indeed can be seen in the high-speed jet that develops from the centre of each grid cell at $(y_g, z_g) = (0, 0)$. While the mean velocity at all three other measurement positions—which are all located behind either vertical or horizontal grid bars—have equalized at around $x_g = 10M$, the high speed jet is rather unaffected by the grid-bars' wakes and only slowly adapts to the other velocities. It is noted, however, that this observed inhomogeneity is mainly limited to the mean-flow distributions, while the RMS distributions in Fig. 6$\mathrm{a_{II}}$ are much more homogeneous for about $x_g \ge 10M$ and decay in streamwise direction. The comparison of our results with the power-law decay presented in Eq. (7) is not the subject of this study, as the decay of non-homogeneous FST downstream of grids is a topic that has been the

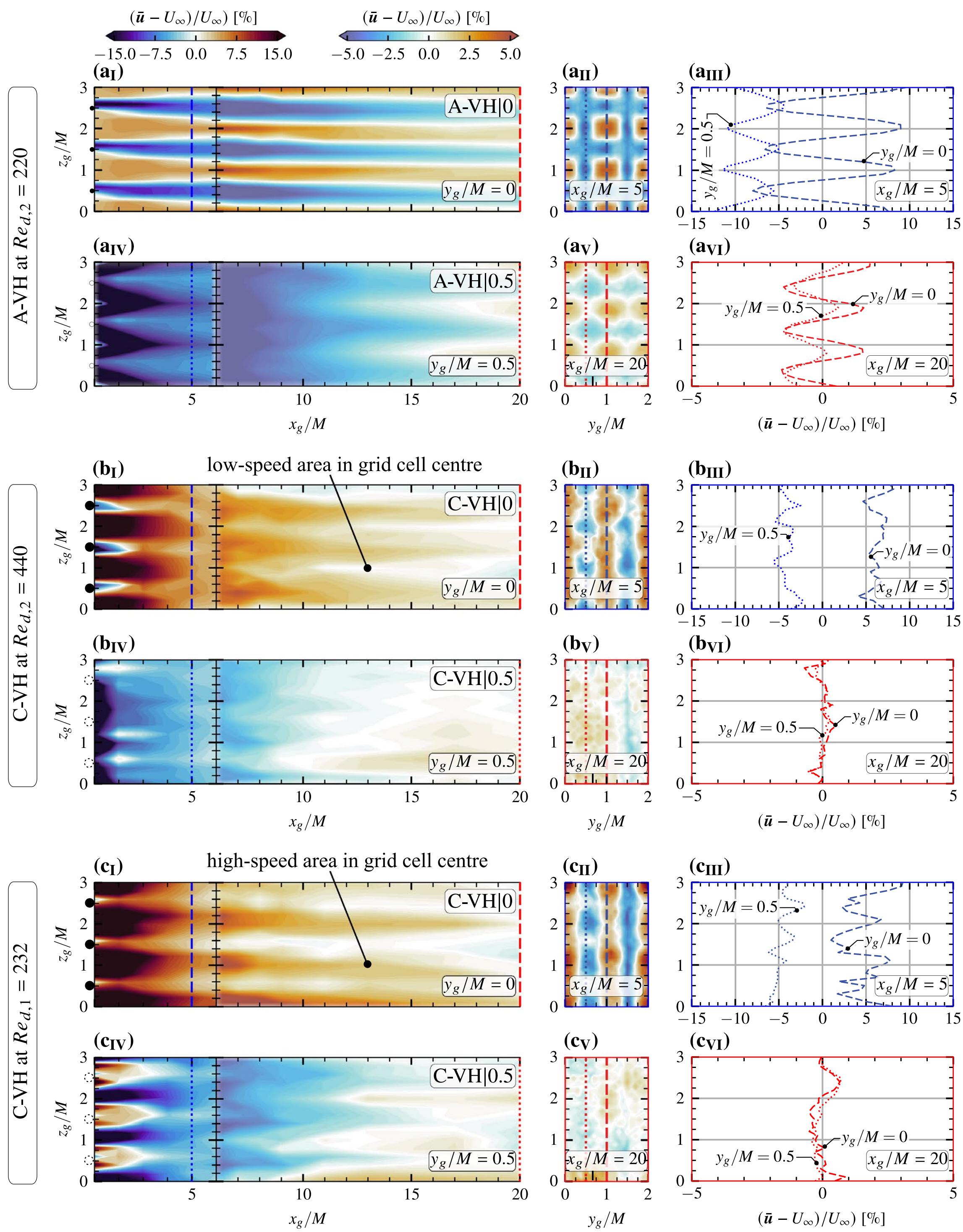

Fig. 5 Mean velocities in the free-stream evaluated from X-probe measurements for setup A-VH at $Re_{d,2} = 220$ (top), setup C-VH at $Re_{d,2} = 440$ (middle), setup C-VH at $Re_{d,1} = 232$ (bottom). The top plane (left row) is measured in $\Delta z_g = 0.2M$ and $x_g = \{1, 2, 3, 4, 5, 6, 7, 8, 9, 11, 13, 17, 20\}M$ steps between two horizontal bars (index I) and behind a horizontal bar (index IV); the front plane (middle row) has a spatial resolution of $\Delta y_g = \Delta z_g = 0.1M$ and is given at $x_g = 5M$ (index II) and $x_g = 20M$ (index V); the spanwise direction (right row) is measured in $\Delta z_g = 0.1M$ steps at $x_g = 5M$ (index III) and $x_g = 20M$ (index IV). In the contour plots and line plots, the averaging time is 60 sec and 600 sec, respectively. The wall-normal positions are given by the dashed lines: $y_g = 0$ and dotted lines: $y_g = 0.5M$; and the streamwise positions are given by blue plots/lines: $x_g = 5M$ and red plots/lines: $x_g = 20M$. Two different contour levels represent the mean velocities in the region $0 < x_g/M \leq 6$ (wider velocity range) and $6 < x_g/M \leq 20$ (narrower velocity range)

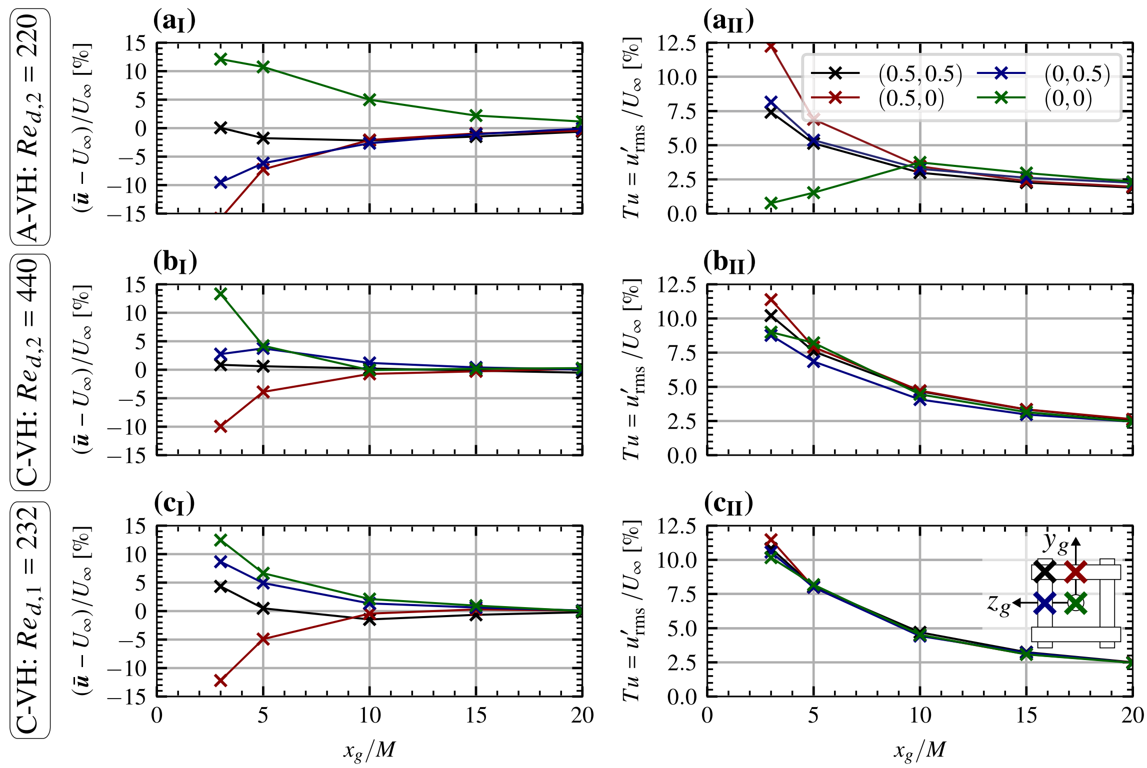

Fig. 6 Mean velocity (left column, index I) and Tu (right column, index II) in the free-stream, evaluated from X-probe streamwise measurements with setup A-VH at $Re_d = 220$ (top row, **a**), C-VH at $Re_d = 440$ (middle row, **b**) and C-VH at $Re_d = 232$ (bottom row, **c**). The averaging time is 600 sec for each setup

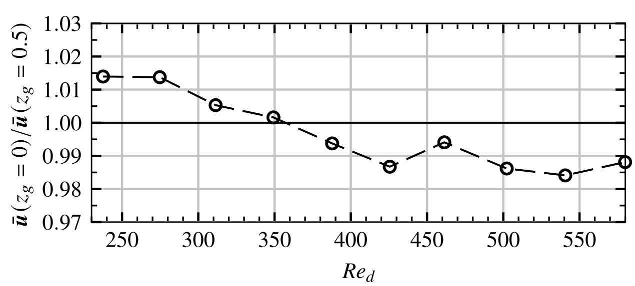

Fig. 7 Low-speed $(\bar{u}(z_g = 0)/(\bar{u}(z_g = 0.5) < 0)$ and high-speed $(\bar{u}(z_g = 0)/(\bar{u}(z_g = 0.5) > 0)$ FS jets evaluated with setups C-VH|0 (circles) and C-VH|0.5 (triangles) depending on Re_d

subject of considerable debate and requires a dedicated investigation.

4.2.3 Influence of the grid diameter d

This section compares the flow field of the C-VH grid ($d = 4$ mm) with that of the previously described A-VH grid ($d = 2$ mm), which differ only in the bar diameter. As already shown in the visualizations in Fig. 4, the larger grid diameter of grid C-VH leads to a significantly stronger mixing of the flow field behind the turbulence grid. As a result, the top view in Fig. 5b$_\mathrm{I}$ shows a much faster mixing of the flow field in the spanwise direction, which causes the mean flow to be virtually homogeneous in the spanwise direction at $x_g = 20M$; this holds for both C-VH|0 and C-VH|0.5. Interestingly, however, the wake of grid C-VH shows a strong layering in the wall-normal direction (see Fig. 5b$_\mathrm{II}$), with low-speed layers at levels behind horizontal bars and high-speed layers in between (see Re_d influence in Fig. 7). This behaviour seems to be a direct consequence of the vertical–horizontal grid order, for which the wakes of the secondly flown-through horizontal grid bars dominate the flow field close to the turbulence grid. Note that this effect was not seen for the A-VH grid with smaller diameter d (Fig. 5a$_\mathrm{II}$). However, both Figs. 5b and Fig. 6b$_\mathrm{I}$ suggest that this layering is mainly a near-grid effect and disappears almost completely for grid distances larger than about $x_g = 15M$, where the flow field can be considered rather homogeneous. Finally, assessing the RMS values in Figs. 6b$_\mathrm{II}$,c$_\mathrm{II}$ of grid C-VH, the RMS values are already at a comparable level for all four evaluation points at $x_g = 3M$, which is the main reason for the faster homogenization of the mean flow field.

It is known that a higher grid diameter generates a higher *Tu* (Batchelor and Townsend 1948), which can be confirmed for almost all measured grid positions upstream of $x_g = 20M$ with Fig. 6a$_{\text{II}}$ and b$_{\text{II}}$. However, the *Tu* values converge towards $Tu = 2.5\,\%$ at $x_g = 20M$, which can be obviously attributed to the strong inhomogeneity with grid A.

4.2.4 Influence of the grid-orientation order

So far, only the VH order of the bars has been analysed. As changing the grid order essentially only represents a turning-by-90-degrees of a setup (e.g. A-VH to A-HV) for the flow field behind the grid ($0 < x_g < 20M$), the results of the different orientation order can be derived from the previous documentation. A comparison of Fig. 5a$_{\text{II}}$ and c$_{\text{II}}$ shows that a 90-degree rotation only has a qualitative influence with grid C, i.e. for a higher d (lower porosity). However, even with grid C, the influence of the orientation order is limited to the near field (approx. $x_g < 15M$), resulting in a rotated low-high-low mean velocity layering. As will be elaborated in the following chapter and in the conclusions, the grid-orientation order will be shown to have only a minor influence on the Klebanoff modes that will emerge on the flat plate. Thus, no HV setups will be discussed in this section, whereby the free-stream results of the turned setup C-HV at $Re_{d,1} = 232$ are given in Appendix 1 for the sake of completeness.

4.2.5 Note on the integral length scale

As introduced in Sect. 2.2, the laminar–turbulent transition due to FST is highly sensitive to the integral length scale, which can vary greatly for different grid configurations. Thus, as a base for further discussion in the following section, both the homogeneity and the absolute value of the integral length scale in the streamwise direction at different spanwise or wall-normal positions $\Lambda_x(y, z)$ is evaluated (see e.g. Lavoie et al. (2007)). In accordance with the study by O'Neill et al. (2004), a truncation value of $1/e$ is used for $f(\tau)$ in Eq. (2); note that the results are qualitatively the same if, for e.g. 0.1 or a zero crossing were used for the truncation, but lower truncation values led to a higher fluctuation of the integral length scale.

In Fig. 8, the spanwise distribution of the resulting Λ_x values is depicted at the streamwise positions **a** $x_g = 5M$ and **b** $x_g = 20M$. Two data series are shown for grids A and C in the vertical–horizontal order, respectively, one analysed at the height behind a horizontal bar and one between two horizontal bars. From Fig. 8a, the length scale

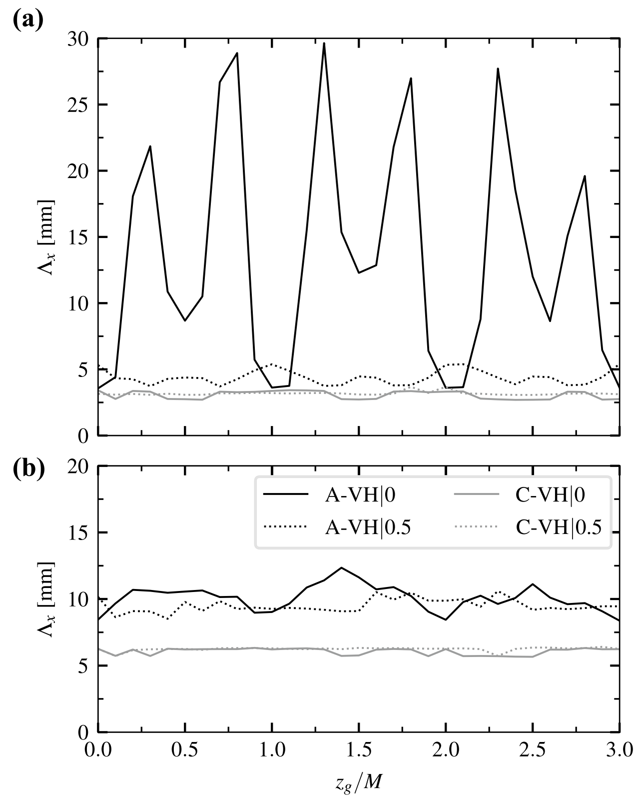

Fig. 8 Integral length scale in the free-stream at streamwise position **a** $x_g = 5M$ and **b** $x_g = 20M$

is relatively similar at the different spanwise positions for setups A-VH|0.5, C-VH|0 and C-VH|0.5, as expected for grids with an identical grid spacing (Fransson and Shahinfar 2020), whereby an intense, periodic, bar-dependent spanwise inhomogeneity is observed for setup A-VH|0. Downstream in Fig. 8b, the absolute length scales have grown for setups A-VH|0.5, C-VH|0 and C-VH|0.5, as expected and described in Sect. 2.3; and with setup A-VH|0, the inhomogeneity is decreased but still present. Overall, this behaviour is consistent with all previous results and merely reflects the fact that the wall-normal mounting position of grid A has a remarkable influence on the free-stream. For grid C, in contrast, a rather homogeneous FST is found at $x_g = 20M$. Interestingly, at $x_g = 20M$ the absolute integral length scale is slightly higher with grid A than with grid C, although Fransson and Shahinfar (2020) showed that for similar grid spacings but different bar diameters rather similar length scales can be expected. Obviously, the intensive inhomogeneity at $x_g = 5M$ for grid A-VH|0 causes a stronger increase of the length scale behind a horizontal bar compared to the one with grid C.

5 Results in the boundary layer

This section discusses to what extent the streaks/Klebanoff modes developing in the laminar boundary layer are influenced differently by the grid configurations installed. All following results are observed at $U_{\infty,2}$. First, the timewise behaviour Sect. 5.1 and the wavelength Sect. 5.2 of the boundary-layer streaks are addressed. In Sect. 5.3, the ones generated by grid B are described.

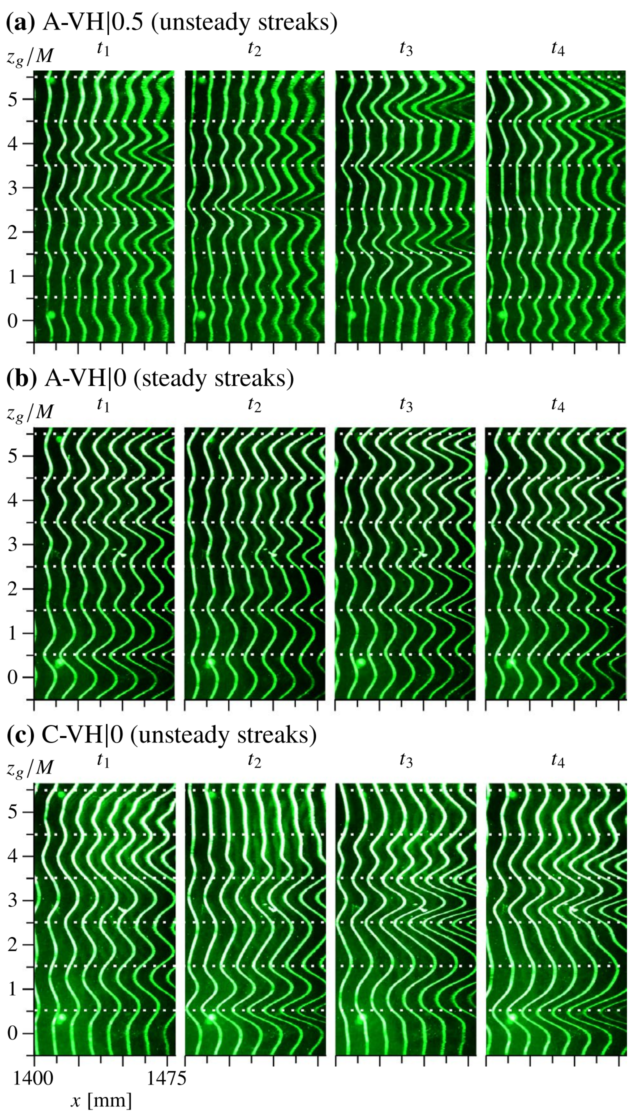

Fig. 9 Hydrogen-bubble visualizations of the boundary-layer streaks with setups: **a** A-VH|0.5 (unsteady streaks), **b** A-VH0 (steady streaks) and **c** C-VH|0 (unsteady streaks), where the hydrogen-bubble wire is located at $(x, y) = (1400\ \mathrm{mm}, 1.4\delta_1)$ (left edge of each snapshot). The snapshots are recorded with a sampling period of 20 s

5.1 Assessment of the streak unsteadiness

5.1.1 Visualizations

For a first insight, Fig. 9 shows hydrogen-bubble visualizations taken $x = 1400$ mm downstream of the plate's LE. The wall-normal position is $y = 1.4\delta_1$ where the maximum u'_{rms} is expected according to Westin et al. (1994); Matsubara and Alfredsson (2001). The results were, however, found to be rather insensitive to the wall-normal position; measurements between about $0.5 < y/\delta_1 < 2.2$ show comparable results. Figure 9 shows a sequence of four snapshots for each case, with a sampling period of 20 s; this corresponds to 362 time units $\delta_1/U_{\infty,2}$. The upstream position of the vertical bars is indicated by the white dotted lines. For case A-VH|0.5, shown in Fig. 9a, the position of the (low-speed) streaks clearly varies across the snapshots in the spanwise direction, indicating a pronounced meandering motion as expected. The spanwise streak spacing varies also, showing streaks of small and large spanwise extent. For the upwards-shifted-grid case A-VH|0, shown in Fig. 9b, the meandering of the streaks is almost completely absent; they only vary in width somewhat and their spanwise spacing λ_z seems to be locked to $M = 25$ mm. Evidently, the stationarity of the streaks in setup A-VH|0 results from the finding already observed in Fig. 4a that the free-stream at the plate's LE is not yet homogeneous for grid A, especially behind the grid cell centres where distinct high-speed streaks are still present. To get a feeling of how sensitive the non-stationarity of the streaks is to the inhomogeneity of the free-stream, the same setup as shown in Fig. 9b for grid A is re-evaluated for grid C in Fig. 9c, for which the free-stream has been shown to be much more homogeneous compared to grid A in Fig. 4c. From Fig. 9c, the BL streaks for grid C with increased grid diameter d are again clearly unsteady, which confirms the expected results that the unsteadiness of the BL streaks strongly depends on the grid diameter selected, respectively Re_d. Moreover, a comparison between panel c and panel a suggests that the maximum wavelengths of the BL streaks generated by grid C are slightly larger compared to grid A, a more detailed discussion is given in Sect. 5.2.

5.1.2 Hot-film measurements

To analyse the spanwise homogeneity of the BL streaks more quantitatively, hot-film measurements are taken at $(x, y) = (900\ \mathrm{mm}, 1.4\delta_1)$ (500 mm upstream of the visualizations in Fig. 9), see Fig. 10, where the spanwise direction was traversed in $\Delta z = 0.12M$ increments and the velocities averaged over a time of 300 s, corresponding to about 500 $\delta_1/U_{\infty,2}$ units per spanwise position. Thus, the homogeneity of the averaged-velocity field is of interest; randomly

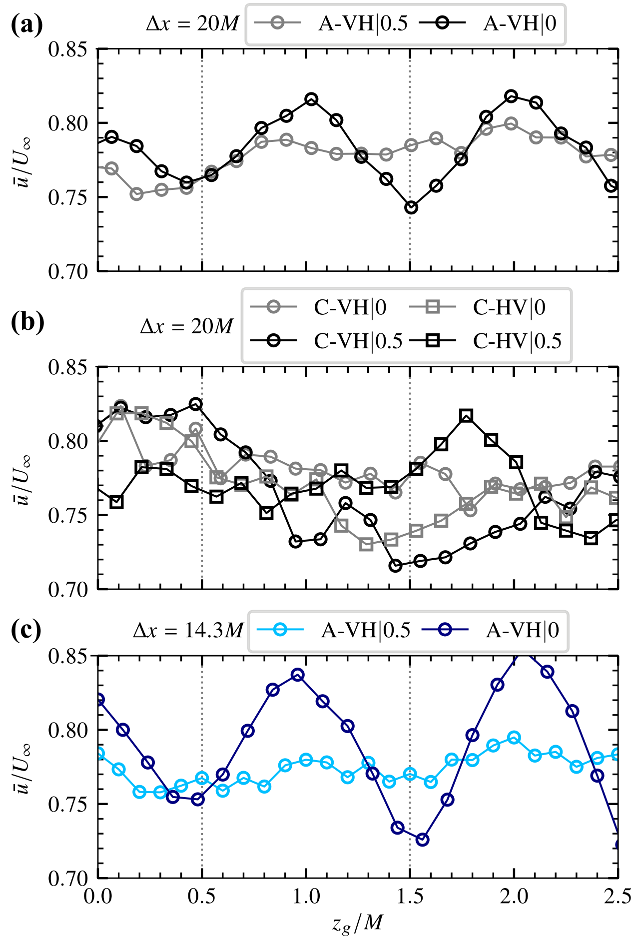

Fig. 10 Mean velocity of hot-film measurements at $(x, y) = (900\,\text{mm}, 1.4\delta_1)$ for different setups, where the distance between the grids and the LE is either **a**,**b** $\Delta x = 20M$ or **c** $\Delta x = 14.3M$

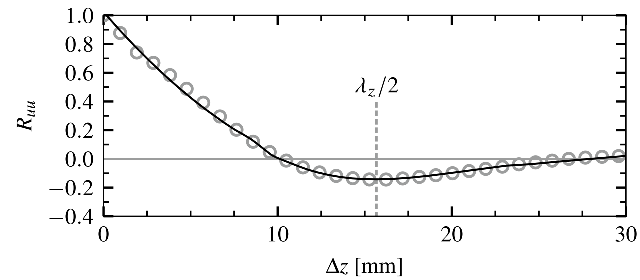

Fig. 11 Two-point spanwise correlation function exemplary shown with setup C-VH|0.5 at $(x, y) = (900\,\text{mm}, 1.4\delta_1)$. The streamwise distance between the grid and the leading edge is $\Delta x = 20M$

meandering streaks cancel largely out, spanwise (almost) locked ones do not.

Figure 10a shows the mean velocity for setups A-VH|0 and A-VH|0.5 for a streamwise grid position of $\Delta x = 20M$. If the flat plate is positioned at the height of a horizontal grid bar, the signal varies slightly only, meaning that largely meandering streaks form in the boundary layer (A-VH|0.5, grey line); if the flat plate is positioned at the height between two horizontal bars (A-VH|0, black line), stationary streaks can be seen, clearly related spatially to the position of the turbulence grid. Further upstream, at $\Delta x = 14.3M$, panel c, the intensity of the steady spanwise deformation for setup A-VH|0 is even larger, whereas for setup A-VH|0.5 it is again relatively low. This is interesting insofar as Fig. 5 also shows for setup A-VH|0.5 at $x_g = 14.3M$ a clearly recognizable, non-homogeneous far-field flow. However, this inhomogeneity seems to be too weak to cause a clear locking of the boundary-layer streaks.

Referring to A-VH|0, the streaks' spanwise wavelength λ_z is about the typical spanwise distance of the maximum or minimum mean velocity peaks. This wavelength ranges within $24 - 26\,\text{mm}$ and thus correlates well with the $M = 25\,\text{mm}$ for both streamwise grid positions $x = -14.3M$ and $-20M$. From Fransson and Shahinfar (2020) it is known that the spanwise wavelength of the streaks varies with the values of both Λ_x and Tu at the LE of the flat plate, which is different in panels a and c, see e.g. Fig. 6; the fact that λ_z of the streaks remains constant here in panels a and c can be taken as an additional indication that the streak spacing in A-VH|0 is actually locked to M.

A final evaluation of grid C in Fig. 10b confirms the already expected results. Although the mean velocity varies relatively strongly in the spanwise direction, it does not show any clear spanwise distribution that could indicate a grid dependency within the boundary layer; this holds for all grid orders evaluated (circles/rectangles in Fig. 10b) as well as for all wall-normal positions of the turbulence grid (black/grey lines in Fig. 10b). Presumably, the strong fluctuations with grid C are caused by the higher streak amplitude, compare Fig. 9a and b with panel c.

5.2 Influence on the Klebanoff mode's wavelength

While the spanwise spacing for the partly appearing steady streaks was determined above, this section investigates the extent to which λ_z of the occurring unsteady streaks/Klebanoff modes differs for the various grid configurations. To this end, PIV measurements of wall-parallel planes within the boundary layer were taken for all investigated turbulence grids, and (the time averaged) λ_z is determined by means of two-point correlations as shown by Mandal et al. (2010). In contrast to an equally possible determination using two probes (see Matsubara and Alfredsson (2001) and Fransson and Shahinfar (2020)), PIV measurements have a significantly reduced measurement time. The measurements are taken in the (x, z)-plane at

$(x, y) = (900\,\mathrm{mm}, 1.4\delta_1)$ ($y = 7\,\mathrm{mm}$) and covered a measurement window of $\Delta x \times \Delta z \approx 59\,\mathrm{mm} \times 74\,\mathrm{mm}$ (spanwise discretization of 0.95 mm). In total, $6 \times 180 = 1080$ double images are recorded for each setup. To identify the streak wavelength, the PIV-based velocity signals are two-point correlated in the spanwise direction for each setup in both positive and negative spanwise direction, with two-point correlation base points at each individual spanwise position. Subsequently, the resulting correlation coefficients are averaged, see Fig. 11 for an exemplary result for setup C-VH|0.5 (grey circles). To slightly smooth the results, a Savitzky–Golay digital filter is then applied to obtain the two-point correlation function $R_{uu}(\Delta z)$ (black line in Fig. 11). Finally, the Δz value of the first minimum of $R_{uu}(\Delta z)$ is identified, which approximately corresponds to half the averaged streak wavelength ($\lambda_z/2$) according to Matsubara and Alfredsson (2001). All calculated wavelengths are given in Table 4.

First, the λ_z value for the steady-streak setup A-VH|0 given in Table 4 is discussed. With about $\lambda_z = 27.4\,\mathrm{mm}$, these values are close to the values of about $\lambda_z = 24 - 26\,\mathrm{mm}$ which have been previously determined from the hot-film measurements, which confirms that the λ_z values determined from the PIV measurements are plausible. Possible reasons for the small deviation between the two values are most likely due to the two-point correlation method itself, for which Alfredsson and Matsubara (2000) noted that it can only approximately determine the streaks' wavelength. Surprisingly, a comparison between grid setup A-VH|0 (stationary streaks) and A-VH|0.5 (meandering streaks) in Table 4 reveals almost the same λ_z values for both setups. The shift of grid setup A in the wall-normal direction by $0.5M$ has obviously influenced only the dominance of either steady or unsteady streaks, and the unsteady averaged streaks in setup A-VH|0.5 seem to be still locked to M. Whether—or how likely—this can be seen as a coincidental match between the grid spacing and the naturally occurring wavelength caused by the turbulence grid will be part of the next section.

From Table 4, the streak wavelengths for setup C-VH|0 ($\lambda_z = 30.2\,\mathrm{mm}$) and C-VH|0.5 ($\lambda_z = 31.2\,\mathrm{mm}$) are slightly higher compared to grid A. As introduced in Sect. 2.2, λ_z can be assumed to be approximately proportional to both Λ_x and Tu, see Eq. (4). Since Tu at the LE is similar for both grids A and C (see Fig. 6), but Λ_x is higher with grid A (see Fig. 8b), Eq. (4) predicts a larger λ_z value, see below, for grid A compared to grid C. However, this prediction contradicts the here observed lower λ_z value with grid A, which is M. If finally the influence of the grid-orientation order is assessed for grid C, compare values for grid C-HV and C-VH in Table 4, only a minor influence is present, which most likely simply can be traced back to the slightly varying values of Tu between both setups.

Table 4 Evaluated streak wavelengths at $(x, y) = (900\,\mathrm{mm}, 1.4\delta_1)$ for the different setups, where the corresponding grid is placed always at $\Delta x = 20M$

Setup	λ_z [mm]	λ_z/δ_1
A-VH|0	27.4	5.6
A-VH|0.5	27.1	5.5
C-VH|0	30.2	6.1
C-VH|0.5	31.2	6.3
C-HV|0	29.4	6
C-HV|0.5	29.3	6

5.2.1 Comparison of the wavelengths with the literature

In the previous section, λ_z of the resulting streaks/Klebanoff modes has been found being close to the spacing of the turbulence grids installed. To assess whether this is a matter of chance, the previously determined values of λ_z are compared with expected values from the literature in the following. The wavelength λ_z is summarized in Table 4 in multiples of the local displacement thickness δ_1 measured at $x = 900\,\mathrm{mm}$. With values between $\lambda_z = 5.6 - 6.3\delta_1$, these values are well in the range of $\lambda_z = 6\delta_1$ as postulated by Matsubara and Alfredsson (2001) for comparable Reynolds numbers, which thus confirms that the measured values for λ_z are plausible, see Sect. 2.2.

In the more recent estimation proposed by Fransson and Shahinfar (2020), see Eq. (4), both Tu and the integral length scale Λ_x at the LE are considered as determining parameters for λ_z, see Sect. 2.2. Recall that estimation (4) does not include a boundary-layer scale and may thus have limited applicability. Exemplarily evaluated for the unsteady setup A-VH|0.5 and setup C-VH|0.5, λ_z is estimated to be about $\lambda_z = 65\,\mathrm{mm}$ and $\lambda_z = 86\,\mathrm{mm}$, respectively, which largely exceeds the measured values in Table 4. One possible reason for this behaviour may be that Eq. (4) does not cover the Re_{FST} range of the water channel under consideration, which, with values of Re_{FST}(A-VH|0.5) = 27 and Re_{FST}(C-VH|0.5) = 20, is about one order of magnitude smaller compared to the measurements in air by Fransson and Shahinfar (2020). Additionally, the different interplay of the Strouhal number, respectively, the dominant dimensional frequency $\propto U/d$ that does not depend much on the viscosity, and Reynolds number, decisive for the boundary layer, $\propto Ud/\nu$, could require a re-calibration of Eq. (4) for water channels (or to include an actual boundary-layer scale). For instance, changing c_1 from 186 to 104 leads to estimated wavelengths of λ_z(A-VH|0.5) = 26.8 mm and λ_z(C-VH|0.5) = 32 mm, which are close to the determined wavelengths. Finally, also the higher truncation value of $(1/e)$ for determining Λ_x from Eq. (2) compared to Fransson and Shahinfar (2020) (zero crossing) has a substantial influence on the estimated wavelength, although it cannot be regarded as the only reason for the observed discrepancy.

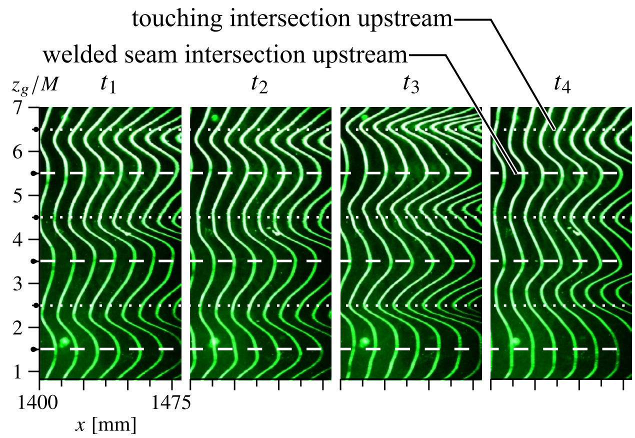

Fig. 12 Hydrogen-bubble visualizations of the boundary-layer streaks with setup B-VH|0 in the (x, z) plane, where the hydrogen-bubble wire is located at $(x, y) = (1400\,\text{mm}, 1.4\delta_1)$ (left edge of each snapshot) and with a time period of $\Delta t = 20\,\text{s}$ between the snapshots

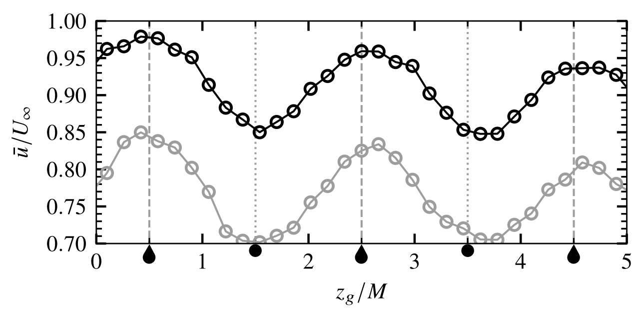

Fig. 13 Mean velocity of hot-film measurements at $(x, y) = (900\,\text{mm}, 1.4\delta_1)$ (grey line) and $(x, y) = (1400\,\text{mm}, 2\delta_1)$ (black line) with setup B-VH|0

5.3 Sensitivity of λ_z to imperfections of the turbulence grids

Obviously, not only the grid geometry itself but also the grid condition greatly influences the characteristics of the FST. A recent study by Zhao et al. (2023) demonstrates, for example, that subsidiary structures in each grid cell intersection or between the intersections can considerably reduce the distance behind a grid downstream of which homogeneity of the FST can be expected. Besides, also inaccurately constructed dual-plane grids or bars roughened with sand grains are reported to notably increase the level of anisotropy/inhomogeneity (Uberoi and Wallis 1967).

Since it is common in practice to manufacture custom grids from welded grid bars for non-purchasable grid specifications, this section examines grid B as an illustrative case, which has been welded together at every second grid node, see Sect. 3.2 and Fig. 2. To evaluate its characteristics, hydrogen-bubble visualizations of the boundary layer are depicted in Fig. 12 analogous to those in Fig. 9 at $(x, y) = (1400\,\text{mm}, 1.4\delta_1)$. Additionally, hot-film measurements are taken at both $(x, y) = (900\,\text{mm}, 1.4\delta_1)$ and $(x, y) = (1400\,\text{mm}, 2\delta_1)$; the resulting mean velocities are given in Fig. 13. In both figures, the spanwise positions of the welded seam intersections are indicated as dashed lines, the positions of the intersections without welded seams as dots. The grid is orientated in vertical–horizontal streamwise order and the flat plate is located at a wall-normal position between two horizontal bars (setup B-VH|0); compared to the previous sections, the grid is placed further upstream at $x = -30M$.

As can be easily seen from both Figs. 12 and 13, the boundary-layer streaks are stationary for all streamwise and wall-normal positions without meandering at all. Moreover, the high-speed streaks occur with great regularity at spanwise positions behind the welded grid nodes, while the low-speed streaks appear behind the non-welded grid nodes. Accordingly, this results in $\lambda_z = 2M$ and thus an approximate doubling. As a consequence, this grid configuration demonstrates that even small imperfections such as tiny welding spots can severely influence the homogeneity and stationarity of the resulting boundary-layer streaks. The welding spots can be considered as an aerodynamic smoothing of the grid bar intersections, causing the free-stream to detach less strongly compared to grid-bar intersections without welding spots. This grid-induced inhomogeneity can persist over very long spatial distances; for the present case, the grid installation position of $\Delta x = 30M$ clearly exceeds the literature's thumb value of $20M$.

6 Conclusions

In this study, the influence of frequently as well as rarely described parameters of turbulence grids on the resulting FST and the Klebanoff modes forming in the boundary layer is investigated. These parameters are: the grid-bar diameter, the associated Reynolds numbers, the grid spacing, the grid porosity, the streamwise distance of the grid to the plate's LE as well as the grid-orientation order, the wall-normal position of the horizontal bars relative to the LE, and the presence of imperfections in the manufactured grids. All experimental setups considered are carried out in a water channel and deal with Reynolds numbers that may be assessed relatively low but are nevertheless representative of a notable number of wind-tunnel experiments from the literature.

General results In general, a comparison between two turbulence grids with same grid spacing M but different porosity β has shown large qualitative differences in the resulting flow fields. For the grid with larger β, i.e. smaller d, the vortex streets forming behind the grid bars are not fully

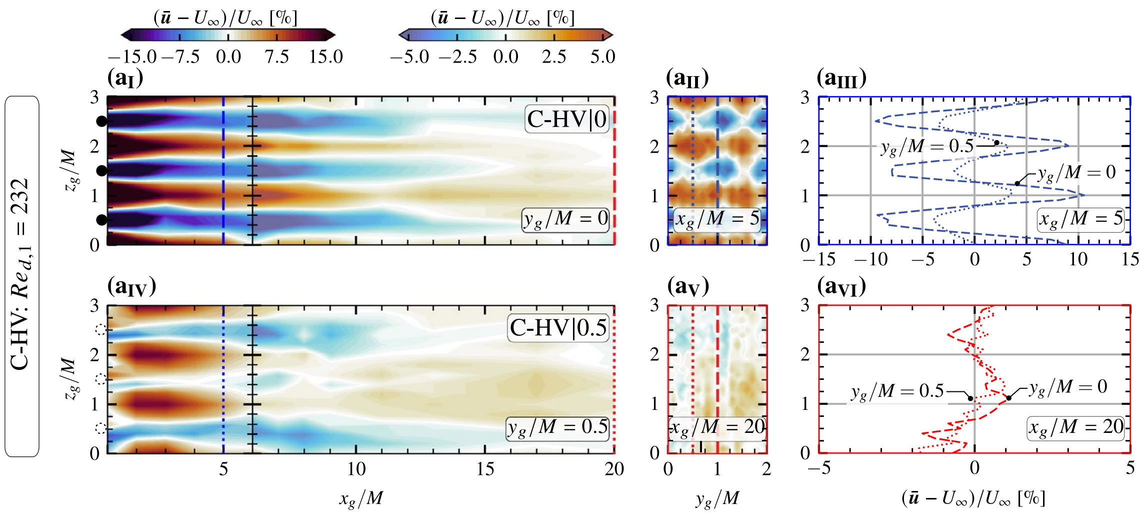

Fig. 14 Mean velocities in the free-stream evaluated from X-probe measurements for setup C-HV at $Re_{d,1} = 232$. See caption from Fig. 5 for details of the plot

mixed even at $x_g = 20M$, a common value where homogenization is usually assumed. Especially at heights between two horizontal bars, the free-stream is characterized by a bar-dependent, spanwise-periodic distribution of both the streamwise mean flow velocity and the integral length scale Λ_x. As these inhomogeneities are far less pronounced at heights behind horizontal bars, where appropriate mixing is already achieved close to the bar, the wall-normal mounting position of turbulence grids with small *d*/*M* (high porosity β) ratio takes on great relevance: (1) If the LE of the flat plate is mounted at heights between two horizontal bars, the Klebanoff modes developing in the laminar boundary layer can become rather steady and both spatially and temporally locked to the grid spacing. (2) If the LE of the flat plate is mounted at the height of a horizontal bar, in contrast, the Klebanoff modes meander in the spanwise direction as expected while showing spatially varying wavelengths. The wavelength was found to match the estimation proposed by Matsubara and Alfredsson (2001) that depends on the boundary-layer displacement thickness, whereas the prediction by Fransson and Shahinfar (2020), not depending on a boundary-layer scale, gave far too large values.

Grid-orientation order Especially for grids with low porosity, it has been shown that the grid-orientation order (horizontal bars/vertical bars or vice versa) can have a significant influence on the FST. Essentially, the trailing bars determine the irregularity/modulation of the mean velocity field in the wake region. If the trailing bars are arranged horizontally, the wake tends to be layered horizontally; if the trailing bars are arranged vertically, the wake tends to be layered vertically. Even if the grid-orientation order was found to only have a minor influence on the Klebanoff mode behaviour for the grids investigated, it cannot be excluded that this feature becomes significant for disadvantageously selected grid configurations or setups in which a grid spacing of $x_g \geq 20M$ cannot be guaranteed due to constructional reasons.

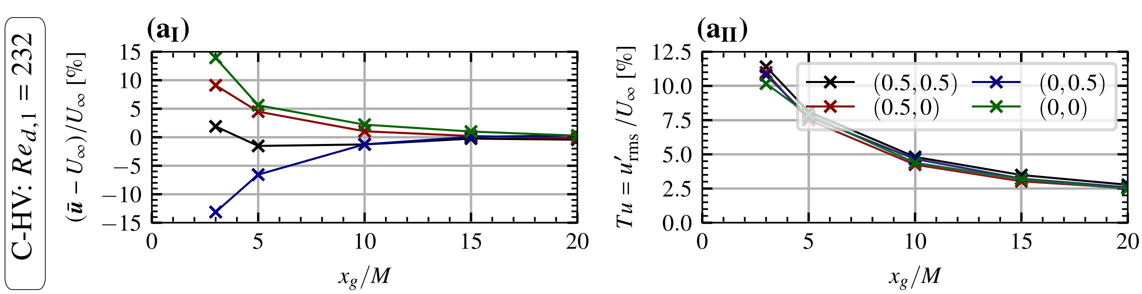

Fig. 15 Mean velocity (left column, index I) and *Tu* (right column, index II) in the free-stream, evaluated from X-probe streamwise measurements with setup C-HV at $Re_{d,1} = 232$. The averaging time is 600 sec

Imperfections of the grids Representative for minor manufacturing-related irregularities, a grid with small welded seams on every second grid cell was investigated. Since the weld seams act like aerodynamic mouldings, high-speed streaks develop in their downstream regions. The influence of these high-velocity regions is extreme and determines the behaviour of the resulting Klebanoff modes even if the distance between the grid and the LE is $\Delta x = 30M$. If the LE is located between two horizontal bars, for instance, uniform stripes are created in the boundary layer, which are clearly fixed to the spanwise welding points' positions.

The results of this study emphasize that FST generated by turbulence grids can have a relatively persistent memory of the turbulence grid through which it was generated; this especially holds for the relatively low-Reynolds-number range investigated within this study. Even if general grid-design guidelines from the literature are followed, the expected behaviour of Klebanoff modes cannot be predicted with certainty, since grid parameters that are commonly not considered, such as the grid-orientation order and mounting height of the grid, also considerably influence their behaviour. It is therefore concluded that the influence of these and other so-far undetermined factors may be one of the reasons why different FST characteristics are observed in the literature for grids with wall-parallel structures. Based on these indications, the authors of this paper consider it advisable that experimental studies on FST especially in the lower Reynolds-number range—analogous to a grid convergence study in numerical investigations—should (i) demonstrate the homogeneity in the free-stream in both spanwise and wall-normal directions, (ii) document the unsteady appearance and wavelengths of the generated Klebanoff modes, (iii) and thus (implicitly) document the spanwise independence of the measurement results.

Best practice guide Based on the results obtained, the following best practice guide seems reasonable to obtain homogeneous FST and meandering Klebanoff modes:

- For grids with higher porosity β, the distance between the grid and the LE of the plate might be required to be larger than $20M$.
- It is preferable to mount turbulence grids in horizontal-bars/vertical-bars order in streamwise direction to avoid inhomogeneity in the spanwise direction.
- If grids are installed with 'regular' imperfection features like spot-welded seams, a characterization of the resulting flow field is even more appropriate.
- Aligning the horizontal bars of the grid to the flat plate's LE helps to enforce unsteady streaks in the boundary layer. Note, however, that inhomogeneities in the *y*/*z*-plane might still affect the transitional boundary-layer's characteristics, implying that grids that do not provide homogeneous FST for sure should not be applied, especially together with isolated roughness elements.

Appendix 1: Free-stream results with setup C-HV at $Re_{d,1} = 232$

Figures 14 and 15 show the free-stream results for setup C-HV similar as described in Sect. 4 with Figs. 5 and 6. The figures confirm that setup C-HV corresponds to a 90-degree rotation of setup C-HV around the x_g-axis. Accordingly, the orientation order of the bars with grid C has a large influence on the homogeneity in the free-stream, but only upstream of $x_g = 20M$.

Acknowledgements We gratefully acknowledge the help of Claudius Elsner and Bernd Peters in carrying out the experiments.

Author Contributions All authors contributed to the study conception and design. Material preparation, data collection and evaluation were performed by T.R., whereby analysis was performed by all authors. The first draft of the manuscript was written by T.R. and C.W. and all authors commented on previous versions of the manuscript. All authors read and approved the final manuscript.

Funding Open Access funding enabled and organized by Projekt DEAL. This work was funded by the Institute of Aerodynamics and Gas Dynamics.

Data availability No datasets were generated or analysed during the current study.

Declarations

Conflict of interest The authors declare no competing interests.

Ethical approval Not applicable.

References

Alfredsson P, Matsubara M (2000) Free-stream turbulence, streaky structures and transition in boundary layer flows. American Institute of Aeronautics and Astronautics, Reston, Virigina. https://doi.org/10.2514/6.2000-2534

Andersson P, Brandt L, Bottaro A, Henningson DS (2001) On the breakdown of boundary layer streaks. J Fluid Mech 428:29–60. https://doi.org/10.1017/S0022112000002421

Batchelor and Townsend (1948) Decay of isotropic turbulence in the initial period. Proceedings of the Royal Society of London Series A Mathematical and Physical Sciences 193(1035):539–558. https://doi.org/10.1098/rspa.1948.0061

Blair MF, Werle MJ (1980) The influence of free-stream turbulence on the zero pressure gradient fully turbulent boundary layer. United Technologies, United Technologies Research Center
Brandt L, Schlatter P, Henningson DS (2004) Transition in boundary layers subject to free-stream turbulence. J Fluid Mech 517:167–198. https://doi.org/10.1017/S0022112004000941
Camp TR, Shin HW (1995) Turbulence intensity and length scale measurements in multistage compressors. J Turbomach 117(1):38–46. https://doi.org/10.1115/1.2835642
Ellingsen T, Palm E (1975) Stability of linear flow. Phys Fluids 18(4):487–488. https://doi.org/10.1063/1.861156
Fransson JHM, Shahinfar S (2020) On the effect of free-stream turbulence on boundary-layer transition. J Fluid Mech 899:A23. https://doi.org/10.1017/jfm.2020.444
Fransson JHM, Matsubara M, Alfredsson PH (2005) Transition induced by free-stream turbulence. J Fluid Mech 527:1–25. https://doi.org/10.1017/S0022112004002770
Fuchs A, Kharche S, Patil A, Friedrich J, Wächter M, Peinke J (2022) An open source package to perform basic and advanced statistical analysis of turbulence data and other complex systems. Phys Fluids 34(10):101801. https://doi.org/10.1063/5.0107974
Groth J, Johansson AV (1988) Turbulence reduction by screens. J Fluid Mech 197:139–155. https://doi.org/10.1017/s0022112088003209
Gustavsson LH (1991) Energy growth of three-dimensional disturbances in plane poiseuille flow. J Fluid Mech 224:241–260. https://doi.org/10.1017/S002211209100174X
Hislop GS (1940) The transition of a laminar boundary layer in a wind tunnel. PhD thesis, University of Cambridge, UK
Hunt JCR, Durbin PA (1999) Perturbed vortical layers and shear sheltering. Fluid Dyn Res 24(6):375–404. https://doi.org/10.1016/S0169-5983(99)00009-X
Jacobs RG, Durbin PA (2001) Simulations of bypass transition. J Fluid Mech 428:185–212. https://doi.org/10.1017/S0022112000002469
Kendall J (1985) Experimental study of disturbances produced in a pre-transitional laminar boundary layer by weak freestream turbulence. In: 18th Fluid Dynamics and Plasmadynamics and Lasers Conference, p 1695.
Kurian T, Fransson JHM (2009) Grid-generated turbulence revisited. Fluid Dyn Res 41(2):021403. https://doi.org/10.1088/0169-5983/41/2/021403
Landahl MT (1980) A note on an algebraic instability of inviscid parallel shear flows. J Fluid Mech 98(2):243–251
Lavoie P, Djenidi L, Antonia RA (2007) Effects of initial conditions in decaying turbulence generated by passive grids. J Fluid Mech 585:395–420. https://doi.org/10.1017/S0022112007006763
Lienhard JH (1966) Synopsis of lift, drag, and vortex frequency data for rigid circular cylinders, vol 300. Bulletin 300, Washington. http://www.uh.edu/engines/vortexcylinders.pdf
Mamidala SB, Weingärtner A, Fransson J (2022) Leading-edge pressure gradient effect on boundary layer receptivity to free-stream turbulence. J Fluid Mech 935:A30. https://doi.org/10.1017/jfm.2022.19
Mandal AC, Venkatakrishnan L, Dey J (2010) A study on boundary-layer transition induced by free-stream turbulence. J Fluid Mech 660:114–146. https://doi.org/10.1017/S0022112010002600
Matsubara M, Alfredsson PH (2001) Disturbance growth in boundary layers subjected to free-stream turbulence. J Fluid Mech 430:149–168. https://doi.org/10.1017/S0022112000002810
Mehta RD (1985) Turbulent boundary layer perturbed by a screen. AIAA J 23(9):1335–1342. https://doi.org/10.2514/3.9089
Mohamed MS, Larue JC (1990) The decay power law in grid-generated turbulence. J Fluid Mech 219(1):195. https://doi.org/10.1017/S0022112090002919
Morkovin MV, Reshotko E, Herbert T (1994) Transition in open flow systems-a reassessment. Bull Am Phys Soc 39:1882
Ohno D, Selent B, Kloker MJ, Rist U (2023) Direct numerical simulation of bypass transition under free-stream turbulence for compressible flows. In: Nagel WE, Kröner DH, Resch MM (eds) High performance computing in science and engineering '21. Springer International Publishing and Imprint Springer, Cham, pp 223–238. https://doi.org/10.1007/978-3-031-17937-2_13
O'Neill PL, Nicolaides D, Honnery D, Soria J, et al. (2004) Autocorrelation functions and the determination of integral length with reference to experimental and numerical data. In: 15th Australasian fluid mechanics conference, vol 1, pp 1–4.
Ovchinnikov V, Choudhari MM, Piomelli UG (2008) Numerical simulations of boundary-layer bypass transition due to high-amplitude free-stream turbulence. J Fluid Mech 613:135–169. https://doi.org/10.1017/S0022112008003017
Puckert DK (2019) Experimental investigation on global instability and critical reynolds number in roughness-induced laminar-to-turbulent transition. PhD thesis, Universität Stuttgart, Stuttgart.
Puckert DK, Dieterle M, Rist U (2017) Reduction of freestream turbulence at low velocities. Exp Fluids 58(5):1–5. https://doi.org/10.1007/s00348-017-2333-y
Puckert DK, Wu Y, Rist U (2020) Homogenization of streaks in a laminar boundary layer. Exp Fluids 61(5):1–15. https://doi.org/10.1007/s00348-020-02947-1
Roach PE (1987) The generation of nearly isotropic turbulence by means of grids. Int J Heat Fluid Flow 8(2):82–92. https://doi.org/10.1016/0142-727X(87)90001-4
Römer TM, Schulz KA, Wu Y, Wenzel C, Rist U (2023) Delay of laminar-turbulent transition by counter-rotating cylindrical roughness elements in a laminar flat plate boundary layer. Exp Fluids 64(2):42. https://doi.org/10.1007/s00348-023-03581-3
Saric WS, Reed HL, Kerschen EJ (2002) Boundary-layer receptivity to freestream disturbances. Annu Rev Fluid Mech 34(1):291–319. https://doi.org/10.1146/annurev.fluid.34.082701.161921
Schlatter P, Brandt L, de Lange HC, Henningson DS (2008) On streak breakdown in bypass transition. Phys Fluids 20(10):101505. https://doi.org/10.1063/1.3005836
Schlichting H (1933) Berechnung der Anfachung kleiner Störungen bei der Plattenströmung. ZAMM 13(171–174):50
Ys Shin, Rist U, Krämer E (2015) Stability of the laminar boundary-layer flow behind a roughness element. ExpFluids 56(1):1–18. https://doi.org/10.1007/s00348-014-1878-2
Tan-Atichat J, Nagib HM, Loehrke RI (1982) Interaction of free-stream turbulence with screens and grids: a balance between turbulence scales. J Fluid Mech 114(1):501. https://doi.org/10.1017/S0022112082000275
Tollmien W (1928) Über die Entstehung der Turbulenz. 1. Mitteilung. Nachrichten von der Gesellschaft der Wissenschaften zu Göttingen, Mathematisch-Physikalische Klasse 1929:21–44. http://eudml.org/doc/59276
Uberoi MS, Wallis S (1967) Effect of grid geometry on turbulence decay. Phys Fluids 10(6):1216–1224. https://doi.org/10.1063/1.1762265
Westin KJA, Boiko AV, Klingmann BGB, Kozlov VV, Alfredsson PH (1994) Experiments in a boundary layer subjected to free stream turbulence. Part 1. Boundary layer structure and receptivity. J Fluid Mech 281:193–218. https://doi.org/10.1017/S0022112094003083
Wiegand T (1996) Experimentelle Untersuchungen zum laminar-turbulenten Transitionsprozess eines Wellenzuges in einer Plattengrenzschicht. Dissertation, University of Stuttgart, Stuttgart
Williamson CHK (1996) Three-dimensional wake transition. J Fluid Mech 328:345–407. https://doi.org/10.1017/S0022112096008750
Zaki TA (2013) From streaks to spots and on to turbulence: exploring the dynamics of boundary layer transition. Flow, Turbul Combust 91(3):451–473. https://doi.org/10.1007/s10494-013-9502-8

Zhao Y, Yang Y, Li M, Peng Y (2023) Measurements of decaying grid turbulence with various initial conditions. Eur J Mech - B/Fluids 102:46–55. https://doi.org/10.1016/j.euromechflu.2023.07.005

Authors and Affiliations

Tristan M. Römer[1] · Markus J. Kloker[1] · Ulrich Rist[1] · Christoph Wenzel[1]

✉ Tristan M. Römer
roemer@iag.uni-stuttgart.de

[1] Institute of Aerodynamics and Gas Dynamics, University of Stuttgart, Wankelstr. 3, 70563 Stuttgart, Germany